Title: Tidally-Driven Diapycnal Upwelling in a Rough Sloping Canyon

Authors: Chih-Lun Liu (chihlunl@gmail.com), Henri Drake (hfdrake@uci.edu)

Earth System Sciences, University of California Irvine

This preprint was submitted to the Journal of Physical Oceanography for peer review, so the manuscript is not yet peer reviewed.

Tidally-Driven Diapycnal Upwelling in a Rough Sloping Canyon

Chih-Lun Liu,[a] Henri F. Drake,[a]

[a] *Earth System Sciences, University of California Irvine*

Corresponding author: Chih-Lun Liu, chihlunl@gmail.com

ABSTRACT: Turbulent mixing over rough topography shapes abyssal ocean dynamics, yet a gap between large- and small-scale models underscores the need to connect processes across scales. Using three-dimensional large eddy simulations (LES) with quasi-realistic sloping topography from a Brazil Basin canyon, we force an ocean model solely with a barotropic M_2 tide body force, allowing internal waves, instabilities, and turbulence to emerge naturally. With horizontally-periodic boundary conditions, bottom-intensified mixing homogenizes the water column and progressively suppresses water mass transformations. By introducing a mean slope, however, a restratifying cross-slope flow develops to balance this mixing, thus enabling the establishment of a non-trivial quasi-equilibrium state. Subgrid scale turbulent mixing drives a water mass transformation that results in approximately 150 mSv of diapycnal upwelling within the bottom boundary layer (BBL) of a single sloping canyon. Extrapolated globally, such abyssal canyons could collectively contribute substantially to the deep branch of the overturning circulation. Lagrangian particle tracking shows that most particles gain buoyancy and rise from their release positions, consistent with localized diapycnal upwelling near the sills. The correlation between buoyancy change and vertical displacement is strong near the sill, but weak downstream, where a hydraulically controlled overflow causes large vertical excursions with little buoyancy change. An analogous tracer release experiment shows that the tracer-weighted mean buoyancy increases at roughly twice the rate of the particle-ensemble mean, reflecting the diffusive drift that affects the tracer but not the particles.

SIGNIFICANCE STATEMENT: The abyssal ocean drives a key part of Earth's climate circulation, but how deep waters return upward remains unclear. Using high-resolution simulations, we show that tides interacting with sloping topography alone can generate strong mixing and drive upward flow across density surfaces near the seafloor. Our results help bridge the gap between small-scale turbulence and large-scale circulation, offering insights that may improve how abyssal mixing is represented in climate and ocean models.

1. Introduction

The global ocean circulation plays a critical role in regulating Earth's climate by redistributing heat, nutrients, salt, and tracers. To satisfy mass conservation, the formation of waters at high latitudes must be balanced by interior transformations elsewhere. While Munk's (1966) "Abyssal Recipes" highlighted vertical mixing as a mechanism enabling this balance, bottom-intensified mixing is now understood to densify interior waters (Polzin et al. 1997), thereby complementing polar downwelling. Recent theoretical studies resolve this conundrum by proposing that diapycnal upwelling primarily occurs within a thin bottom boundary layer, where intensified turbulent mixing induces upwelling (Ferrari et al. 2016; McDougall and Ferrari 2017; Drake et al. 2020)– a mechanism supported by observations of dye upwelling along slopes in a submarine canyon (Wynne-Cattanach et al. 2024). One essential component of this upwelling is that mixing intensifies near the bottom, as evidenced in turbulence measurements (St. Laurent et al. 2012), which creates differential buoyancy fluxes: in the interior, bottom-intensified mixing causes the lower portion of a water parcel to mix more strongly with denser water below, leading to a net loss in parcel buoyancy and driving it to sink. In contrast, assuming there is no buoyancy flux across the seafloor boundary, a water parcel only mixes with the lighter water above, resulting in a net increase in buoyancy, promoting upwelling.

A large portion of the bottom-intensified mixing arises from the interaction between barotropic tides and rough topography (MacKinnon et al. 2017). Seminal reviews emphasize that the character of internal waves and associated turbulence depends on slope criticality and topographic steepness: near-critical slopes and hydraulic jumps promote strong boundary-layer mixing and energy dissipation, while supercritical topography leads to flow blocking, downslope jets, and hydraulic control (Sarkar and Scotti 2017; Legg 2021). These processes transfer barotropic energy to smaller scales

through internal wave breaking and lee wave generation, sustaining elevated diapycnal mixing near rough topography. Nonlinear wave–wave interactions and geometric focusing enhance dissipation and energy transfer across modes (Polzin 2004, 2009; Muller and Bühler 2009; Vic et al. 2019). Inspired by previous studies that highlighted the role of internal wave dynamics and boundary layer processes in driving mixing (e.g., Nikurashin and Legg 2011; Drake et al. 2022a), our approach takes these ideas further by applying a three-dimensional large eddy simulation (LES) over quasi-realistic sloping topography. Unlike Nikurashin and Legg (2011), we resolve a 3D domain with a geometry that includes both realistic roughness and a mean slope, and unlike Drake et al. (2022a), we drive the system with tidal forcing and allow the turbulent diffusivity to emerge from the LES closure rather than simply prescribing it.

Our study aims to show that barotropic tidal forcing is a critical source of bottom-enhanced mixing, leading to diapycnal upwelling. We focus on a sloping submarine canyon ($\theta = 0.0036$ rad) in the fracture zone of Brazil Basin, inspired by the Dynamics of Mid-Ocean Ridge Experiment (Clément and Thurnherr 2018). Simulations are driven solely by barotropic M_2 tidal forcing, capturing the full spectrum of dynamics from inertial and tidal scales to the full internal wave continuum, providing a natural framework to bridge large- and small-scale processes. Unlike previous numerical studies that prescribe constant bottom-intensified turbulent diffusivity (e.g., Callies 2018a; Drake et al. 2022a; Holmes and McDougall 2020), a turbulent diffusivity is parameterized using Smagorinsky turbulence closure. Although a quasi-realistic topography is used, the objective is not to replicate specific observations but rather to elucidate the underlying dynamics and physical mechanisms governing tidally–driven mixing and diapycnal upwelling within a sloping canyon.

Prior numerical simulations of tidally driven mixing near the seafloor are inherently transient, as the mixing eventually washes away the initial stratification (Nikurashin and Legg 2011; Ruan et al. 2025; Whitley and Wenegrat 2025). This study aims to bridge the gap between small-scale tidal mixing and larger-scale abyssal slope dynamics by examining a regime in which bottom-intensified turbulence is balanced by restratification, sustaining a quasi-equilibrium state of steady near-bottom buoyancy (Phillips 1970; Wunsch 1970; Garrett et al. 1993; Callies 2018a). Barotropic tidal interactions with topography enhance mixing by generating internal waves that break and destabilize the bottom boundary layer. With a sloping seafloor ($\theta = 0.0036$ rad), restratification by a cross-slope mean flow counteracts this mixing, maintaining a stable stratification, in contrast

to non-tilted configurations where mixing leads to transient and persistent homogenization. Our analysis concentrates on the dynamics after this quasi-equilibrium has been established, when buoyancy remains approximately steady near the bottom.

The governing equations in tilted coordinates and the numerical model configuration are described in §2. §3 presents an overview of the internal tide simulation and the establishment of a quasi-equilibrium bottom stratification. Evidence of diapycnal upwelling unique to the sloping seafloor, including the development of an Eulerian upslope mean current within the canyon and associated water-mass transformation, is examined in §4. Analyses of Lagrangian particles and tracer-weighted statistics that further substantiate the diapycnal upwelling mechanism are presented in §5. The paper concludes with a discussion and summary in §6.

2. Numerical Modeling Framework

This section describes the numerical setup for simulating internal tide-driven mixing in a three-dimensional (3D) domain, focusing on a single fracture zone canyon in the Brazil Basin (Fig. 1a). We use Oceananigans.jl (Wagner et al. 2025), a GPU-accelerated finite-volume ocean modeling framework, to solve the non-hydrostatic Boussinesq equations on a staggered, structured grid, capturing multiscale dynamics over quasi-realistic topography.

a. Governing Equations

To model dynamics influenced by sloping topography, we solve the non-hydrostatic Boussinesq equations in a coordinate system rotated by the mean topographic slope angle θ, i.e. $(x, y, z) \equiv (\hat{x}\cos\theta + \hat{z}\sin\theta, \hat{y}, \hat{z}\cos\theta - \hat{x}\sin\theta)$, where the hat symbol denotes quantities in the gravity-aligned coordinates (Wunsch 1970; Phillips 1970; Drake et al. 2022a). This tilted coordinate system, aligns the x-axis with the cross-slope direction, and the governing equations are:

$$u_t + \mathbf{u}\cdot\nabla u - f_0 v\cos\theta = -p_x + b\sin\theta + \nabla\cdot(\nu_T\nabla u) + \mathcal{F}_{\text{tide}}, \tag{1}$$

$$v_t + \mathbf{u}\cdot\nabla v + f_0 u\cos\theta = -p_y + \nabla\cdot(\nu_T\nabla v), \tag{2}$$

$$w_t + \mathbf{u}\cdot\nabla w = -p_z + b\cos\theta + \nabla\cdot(\nu_T\nabla w), \tag{3}$$

$$\nabla\cdot\mathbf{u} = 0, \tag{4}$$

$$b_t + \mathbf{u}\cdot\nabla b + N^2(w\cos\theta + u\sin\theta) = \nabla\cdot\left\{\kappa_T\left[N^2(z\cos\theta + x\sin\theta) + \nabla b\right]\right\}, \tag{5}$$

where $\mathbf{u} = (u, v, w)$ is the velocity vector (cross-slope, along-slope, and slope-normal components, respectively), p and b are the perturbation pressure and buoyancy, $\mathcal{F}_{\text{tide}}(t)$ is a tidal forcing, f_0 is a constant Coriolis parameter, N^2 is the background vertical buoyancy gradient, ν_T is the turbulent viscosity, κ_T is the turbulent diffusivity. Subscripts denote partial derivatives, and ∇ is the gradient operator.

The total buoyancy is decomposed as $B = \bar{B} + b$, where $\bar{B} = N^2\hat{z}$ is a uniformly-stratified background state (in hydrostatic balance with an implicit background pressure $\overline{P}$) and $b(\hat{x}, \hat{y}, \hat{z}, t)$ is the perturbation buoyancy. This decomposition enables periodic boundary conditions in the plane of the slope while accounting for the sloping coordinate system, with $\bar{B}$ only contributing to the advection and diffusion terms [Eq. (5)].

b. Numerical Model and Implementation

The model resolves scales from low-mode internal tides ($\lambda_x \approx 30$ km) to high-mode shear and convective instabilities ($\lambda_x, \lambda_z \approx 10 - 100$ m). The horizontal grid spacing is $\Delta x = \Delta y = 30$ m while the vertical grid spacing stretches from $\Delta z = 7.5$ m near the bottom to 20 m at the top of the domain, yielding a 3D grid of $(500, 1000, 250)$ cells. This is the largest grid that fits in memory on a single A100 GPU. Subgrid-scale turbulence is parameterized using the Smagorinsky-Lilly closure (Smagorinsky 1963; Lilly 1962), which captures unresolved dissipation while preserving spatial and temporal variability. Although the Smagorinsky–Lilly closure is not without limitations, it represents a clear advancement over prior studies that relied on constant diffusivities (Nikurashin and Legg 2011) or prescribed vertical profiles (e.g., Callies 2018a; Drake et al. 2022a), which inherently constrain mixing pathways and suppress natural variability. We evaluate the adequacy of our vertical resolution by comparing the grid spacing with the Ozmidov length scale, L_O, estimated both pointwise and following the formulation of Khani (2018) (Appendix). The comparison demonstrates that our vertical grid spacing is sufficiently fine to resolve the majority of turbulent L_O values, ensuring that the dominant turbulent motions relevant to stratified mixing are explicitly captured within the LES framework. Advection of momentum and tracers employ the 5^{th}-order Weighted Essentially Non-Oscillatory (WENO) scheme, providing implicit dissipation without additional explicit terms (Silvestri et al. 2024). Time stepping uses a third-order Runge-Kutta method.

Horizontal boundaries are periodic in the sloping (x, y) plane. The bottom boundary conditions are free-slip with a quadratic drag (with $C_D = [\kappa_{\text{von}}/\log(z/z_0)]^2$, where $\kappa_{\text{von}} = 0.4$ is the von Kármán constant and $z_0 = 0.1$ m is the roughness length) for momentum and no-normal-flux for mass and total buoyancy. Crucially, the boundary condition of zero normal flux of total buoyancy corresponds to a source of *perturbation* buoyancy, since $\nabla B \cdot \hat{\boldsymbol{n}} = 0$ implies $-\kappa_T \nabla b \cdot \hat{\boldsymbol{n}} = \kappa_T \nabla \overline{B} \cdot \hat{\boldsymbol{n}} > 0$, where $\hat{\boldsymbol{n}}$ is the unit vector normal to the seafloor. The top boundary is free-slip and no-flux for mass, and perturbation buoyancy. The combination of the no-flux condition on perturbation buoyancy ($\partial b/\partial z = 0$) and cross-slope periodicity ($\partial b/\partial x = 0$) guarantees that the solution at the top boundary matches the assumed far-field buoyancy gradient, $\nabla B \cdot \hat{\boldsymbol{z}} = N^2$. This condition maintains a consistent diffusive flux into the domain, $\frac{\partial}{\partial z}\left(\kappa_T \frac{\partial \overline{B}}{\partial z}\right)$, allowing the stratification in the domain to evolve naturally. By contrast, using a sponge layer as in Nikurashin and Legg (2011) would relax the solution towards a prescribed buoyancy field and thus interfere with the equilibration processes of interest.

Tidal forcing is applied as a body force, $U_0\omega_0 \sin(\omega_0 t)$, where $U_0 = 0.025$ m s^{-1} and $\omega_0 = 1.4 \times 10^{-4}$ s^{-1} represent the M_2 tide frequency in the up-slope momentum equation (Eq. 1). The initial velocity field is chosen to match the predicted linear tidal response, with the velocity field set in phase with the forcing (corresponding to low tide),

$$\boldsymbol{u}(x, y, z, t = 0) = \frac{U_0 \omega_0^2}{\omega_0^2 - f_0^2 - (N \sin\theta)^2} \hat{\boldsymbol{x}}. \tag{6}$$

This prevents the excitation of spurious inertial "ringing" that would otherwise arise if the system were started from rest (Nikurashin and Legg 2011). The Coriolis parameter $f_0 = -5.3 \times 10^{-5}$ s^{-1} and $N = 0.001$ s^{-1}, consistent with Brazil Basin observations (Polzin et al. 1997). The tilting angle θ is 0.0036 rad, which is estimated from the mean slope of the topography. It is small but large enough for emergent cross-slope flows to maintain a finite stratification (Drake et al. 2022a).

The initial pressure and buoyancy perturbations are identically zero, leaving just the implicit background pressure in hydrostatic balance with the uniformly stratified background buoyancy field. To reach a statistical equilibrium in which the thickness of the bottom mixing layer begins to converge, the model requires a finite spinup time of roughly 450 tidal periods.

c. *Domain and Bathymetry*

The simulation domain targets a fracture zone canyon in the Brazil Basin, characterized by 30 km-wide canyons and anisotropic abyssal hills, with bathymetry derived from SYNBATH (Sandwell et al. 2022; Gevorgian et al. 2023). The domain spans $(L_x, L_y, L_z) = (15\,\text{km}, 30\,\text{km}, 2.25\,\text{km})$, with the x-axis perpendicular and the y-axis parallel to the mid-ocean ridge, accommodating low-mode internal tides (vertical modes 5–100) and, potentially, submesoscale instabilities (Wenegrat et al. 2018; Callies 2018b). To focus on near-bottom dissipation driven by high vertical wavenumber internal waves, the vertical extent is limited to 2.25 km. The bathymetry features a sloping abyssal canyon section with a transverse ocean ridge and is self-similar, with western and eastern boundaries having canyons of similar width, and southern and northern boundaries marked by taller topographic features of comparable height. The topography is hence already approximately periodic in x and y; we apply filtering to smooth out any residual discontinuities across the boundaries (Fig. 1b).

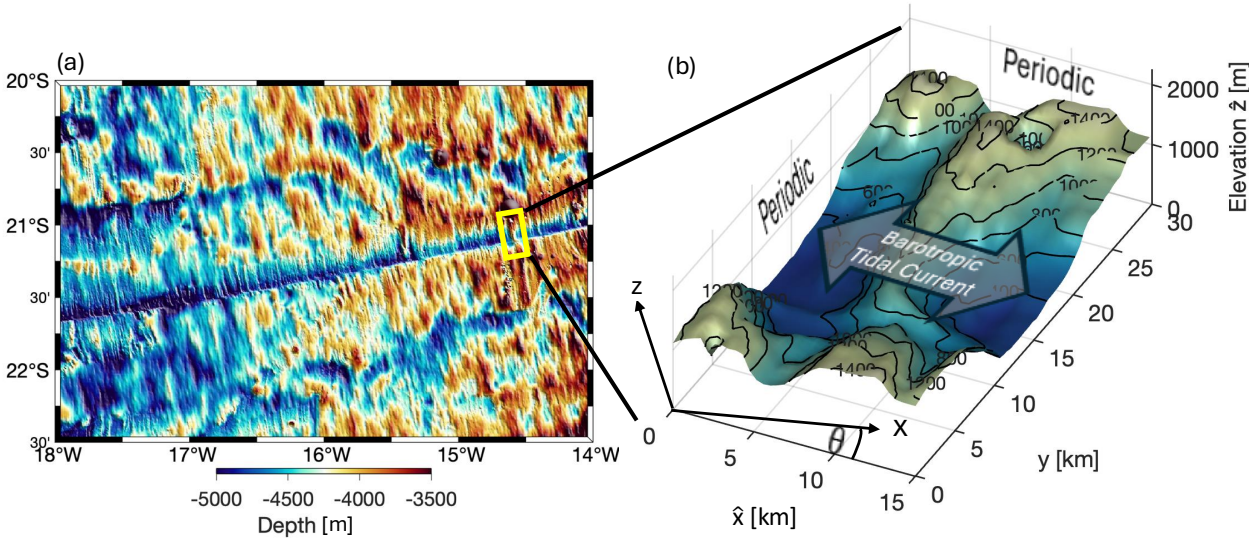

FIG. 1. (a) Bathymetry of the western flank of the Mid-Atlantic Ridge in the Brazil Basin. The seafloor topography exhibits diverse features including submarine canyons, abyssal hills with varying wavelengths and amplitudes, and ridge structures. (b) Three-dimensional representation of the numerical model domain (zoomed view of yellow box in panel a). The barotropic tidal current flows parallel to the submarine canyon, which intersects a topographic ridge at the center of the domain.

3. Internal tide simulation

In the early stage of the simulation ($t = 2$ tidal periods), the interaction between the barotropic tide and bottom topography generates distinct internal wave beams (Fig. 2a,c). These beams align closely with the linear dispersion relations of the tidal harmonics, indicated by the dashed lines, and are characterized by intensified velocity, sharpened buoyancy gradients, and enhanced turbulent kinetic energy dissipation rates (ε). At the later stage ($t = 460$ tidal cycles), the wave field evolves into a more complex state in which individual wave beams are no longer evident (Fig. 2b,d). Instead, the system is marked by layers of strong stratification and elevated dissipation, particularly near blocking sills (A time-evolving visualization of zonal velocity and dissipation rate at late stages is provided in a supplementary movie S1). While the enhanced buoyancy gradient near the upper boundary ($z \sim 2100$ m) may partly arise from unrealistic wave reflection processes at the upper boundary, this artifact does not affect the interpretation of the near-bottom dynamics, which is our main focus.

Overall, the comparison between the initial and later stages highlights a substantial adjustment of the flow field. In the presence of sloping topography, we anticipate that the system will eventually equilibrate, with the near-bottom buoyancy gradient reaching a quasi-steady structure.

a. Buoyancy adjustment

To elucidate the physical mechanisms governing internal tide-driven mixing at equilibrium, we investigate the role of a sloping seafloor in shaping the buoyancy field in a quasi-steady state. We conduct two simulations with identical configurations, differing only in their mean topographic slopes: one with a realistic slope of ($\theta = 0.0036$ rad), representative of the Brazil Basin's fracture zone canyon (Fig. 1b), and a control case with the same topographic roughness but no slope ($\theta = 0$). This comparative approach quantifies the critical role of slope-induced restratification in maintaining near-bottom stratification and demonstrates that pre-equilibrium dynamics may significantly deviate from the equilibrated state characteristic of the natural ocean.

A Hovmöller diagram of the height-above-bottom (HAB) averaged vertical buoyancy gradient, spanning 450 M_2 tidal periods, reveals distinct dynamics between the two cases (Fig. 3). In the sloping case (Fig. 3a), the bottom mixing layer, roughly the bottom 250 m, reaches quasi-equilibrium after approximately 450 tidal periods, with the buoyancy gradient ($\partial B/\partial z$) stabilizing

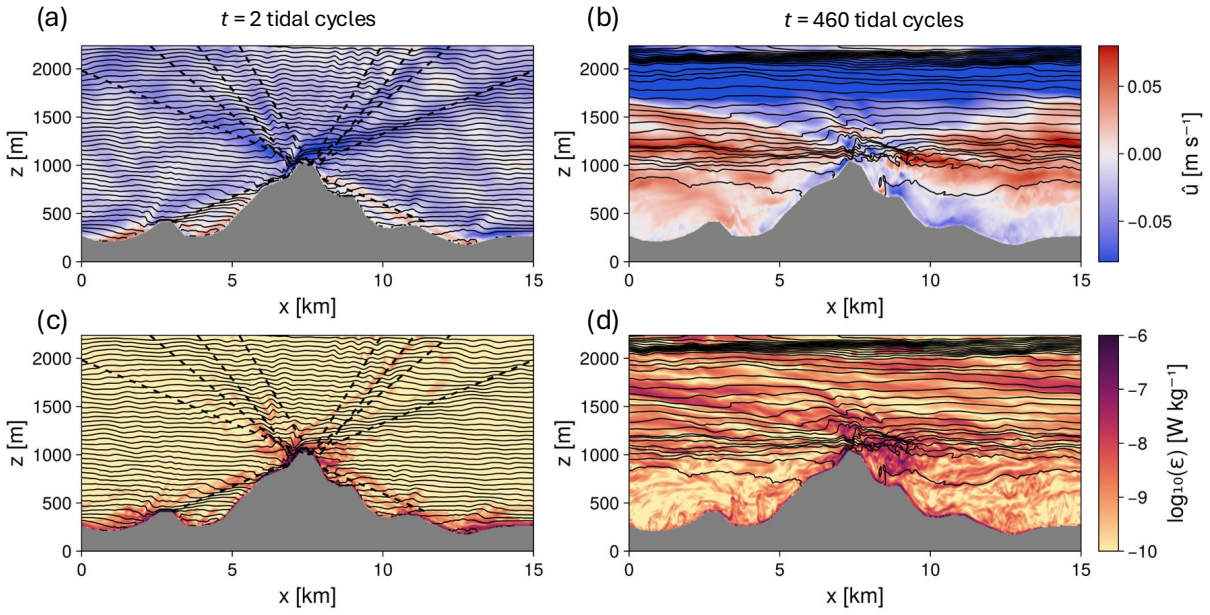

193 FIG. 2. Tidally-driven evolution of an internal wave field and associated turbulence, illustrated through zonal
194 velocity (a,b) and turbulent kinetic energy dissipation rates (c,d) and equally spaced buoyancy surfaces (black
195 contours) for the tilted case. The snapshots depict the system at (a,c) $t = 2$, and (b,d) 460 M_2 tidal periods.
196 Dashed lines represent internal wave beams with different slopes, corresponding to frequencies of ω_0, $2\omega_0$, $3\omega_0$,
197 and $4\omega_0$, from the dispersion relationship. (b,d) Subsequent snapshots during the down-slope phase show the
198 further development of the internal wave field, where distinct internal tide beams become less apparent. Both
199 $t = 2$ and $t = 460$ tidal cycles are at the downslope phase of the tide.

213 due to restratifying advective buoyancy fluxes that counteract the tidally-driven mixing (Drake et al.
214 2022a). In contrast, the flat-bottom case initially mirrors the sloping case's buoyancy gradient for
215 the first 50 tidal periods but diverges thereafter, forming a weakly stratified layer exceeding 700
216 m in thickness (Fig. 3b). This highlights the absence of cross-slope restratification, allowing the
217 tidally-driven turbulent mixing to homogenize the water column indefinitely.

218 The FFT pressure solver employed during the spinup period introduces a minor numerical
219 artifact near the topographic immersed boundary condition, manifesting as an enhanced $\partial B/\partial z$
220 within the BBL (0–40 m) due to spurious normal velocities (and advective buoyancy fluxes) across
221 the seafloor boundary. To ensure accuracy at equilibrium, we switched to the iterative CG solver
222 at 450 tidal periods, which more reliably enforces the no-flux bottom boundary condition. The
223 BBL adjusts rapidly to this switch, governed by a turbulent timescale of approximately 1 hour,

calculated as $\tau_\varepsilon \approx (h^2/\varepsilon)^{1/3}$, where ($h \approx 40$ m) is the BBL thickness and ($\varepsilon \approx 10^{-7}$ m^2 s^{-3}) is the turbulent dissipation rate. This rapid adjustment, driven by vigorous mixing and convective instabilities in the BBL, ensures that one additional tidal cycle (12.47 hours) is sufficient to correct the near-bottom artifacts. Given the BBL's small vertical extent (1.8% of the 2.25 km domain), the artifact has negligible impact on the broader water column. Therefore, all analyses are conducted from 451 tidal periods onward, after the adjustment, ensuring that the results presented are free from boundary artifacts.

The differences between these two simulations underscore the profound influence of subtle seafloor slopes on abyssal mixing processes. By resolving transient and equilibrated dynamics with a robust numerical strategy, this experiment highlights the critical role of topography in sustaining oceanic stratification and mixing.

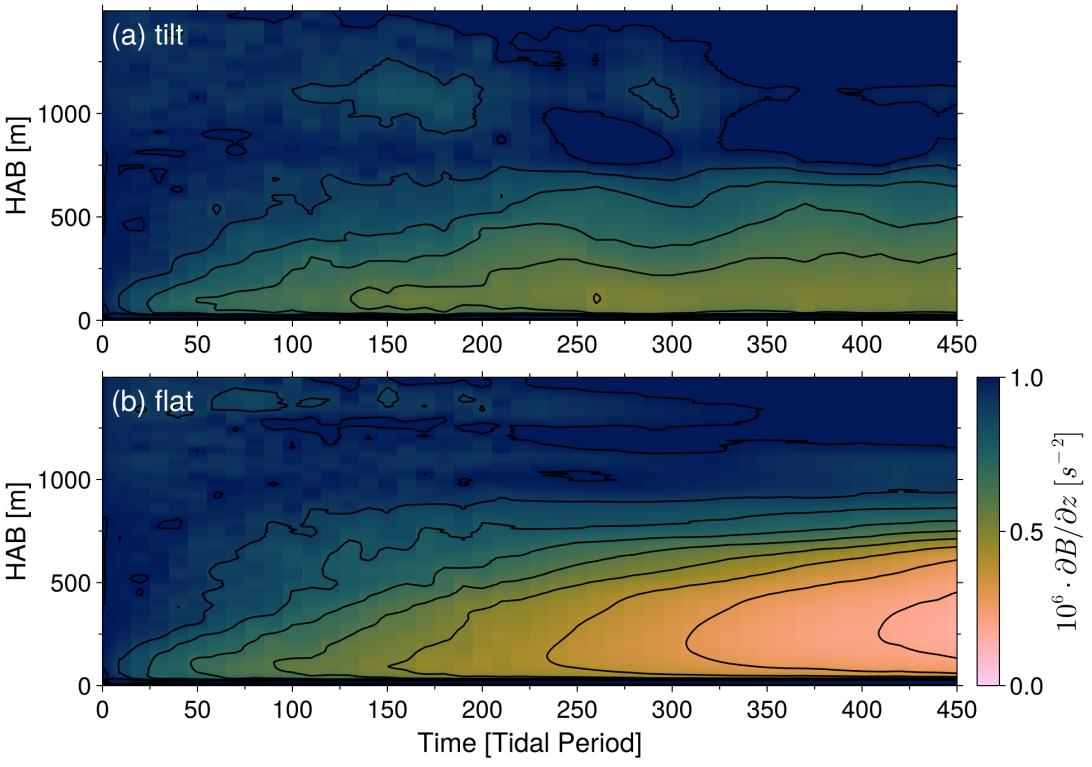

FIG. 3. Height above the bottom (HAB) average and time averaged buoyancy gradient for (a) tilt and (b) flat case. Mixing layer thickness near the bottom converges for the tilt case, but continues to broaden in the flat case.

b. Buoyancy budget

The buoyancy budget provides insight into the mechanisms driving restratification over the sloping seafloor. Starting from the Boussinesq buoyancy equation, we apply a tidal average and decompose the advection term into the mean and fluctuating components,

$$\frac{\partial \overline{B}}{\partial t} = - \underbrace{\nabla \cdot (\overline{\mathbf{u}}\,\overline{B})}_{\text{subtidal mean buoyancy flux}} - \underbrace{\nabla \cdot \overline{\mathbf{u}'B'}}_{\text{tidal eddy buoyancy flux}} - \underbrace{\overline{\nabla \cdot \mathcal{B}}}_{\text{subgrid-scale diffusive buoyancy flux}}, \tag{7}$$

where $\overline{(.)}$ denotes averages over a tidal period ($2\pi/\omega_0$) and $\mathcal{B}$ represents the subgrid-scale turbulent buoyancy flux,

$$\mathcal{B} = -\kappa_T \nabla B. \tag{8}$$

The first term at the right-hand side of Eq. 7 is the subtidal advective buoyancy flux convergence, associated with processes at frequencies lower than the M_2 tide; the second term is the tidal eddy flux convergence, which capture higher-frequency resolved perturbations such as instabilities and internal waves. The final term represents subgrid-scale diffusive flux convergence, parameterizing isotropic turbulent mixing below the Ozmidov scale.

To understand how mixing and advection maintain the near-bottom buoyancy structure, we examine the tidally averaged buoyancy budget. After averaging over ten tidal periods (451-461) as a function of height above bottom (HAB), the system reaches a quasi-steady state in which the buoyancy tendency is negligible, and the primary balance is between turbulent diffusive, subtidal mean, and tidal eddy fluxes (Figure 4a). More than 100 m above the bottom, the turbulent diffusive flux is negligible, leaving a balance between the subtidal mean (blue) and the tidal eddy (green) fluxes. Near the bottom, however, the subgrid-scale turbulent flux (red) is convergent, increasing buoyancy, and indicating time-mean diapycnal upwelling,

$$\overline{\frac{\mathrm{D}B}{\mathrm{D}t}} = -\nabla \cdot \overline{\mathcal{B}} > 0 \tag{9}$$

This upwelling is counteracted by a divergent tidal eddy flux, which reduces buoyancy. The vertical variation of these flux divergences determines the bottom stratification tendency: the convergence of diffusive flux decays with height, $\partial_{\mathrm{HAB}}(-\nabla \cdot \overline{\mathcal{B}}) < 0$, weakening the stratification. The tidal eddy

flux divergence has the opposite trend, $\partial_{\mathrm{HAB}}(-\nabla\cdot\overline{\boldsymbol{u}'B'}) > 0$, acting to restore stratification near the bottom.

The subtidal mean flux is also convergent in the bottom ~ 100 m, i.e., $\nabla\cdot(\overline{\boldsymbol{u}}\,\overline{B}) = \overline{\boldsymbol{u}}\cdot\nabla\overline{B} < 0$. In the Eulerian perspective, this corresponds to a mean velocity directed downward across mean isopycnals,

$$\overline{\boldsymbol{u}}\cdot\frac{\nabla\overline{B}}{|\nabla\overline{B}|} = \overline{\boldsymbol{u}}\cdot\overline{\boldsymbol{n}_B} < 0, \tag{10}$$

where $\overline{\boldsymbol{n}_B}$ is the unit vector normal to the time-mean isopycnals, directed upwards in the time-mean due to the stable stratification. Thus, the mean flow contributes a non-negligible diapycnal downwelling, consistent with the negative mean vertical velocity near the bottom (Fig. 4b). Overall, the near-bottom buoyancy balance is maintained by a close competition between the turbulent diffusive flux convergence and the tidal eddy flux divergence, while the mean downwelling modulates this balance and influences the stratification of the boundary layer. Mechanistic explanations of the time-mean near-bottom downwelling and the tidal eddy fluxes will be analyzed in greater detail in future work. While the time-mean height-above-bottom-averaged flow is downhill, the following section shows that the Eulerian mean, residual mean, and Lagrangian mean transport are all uphill.

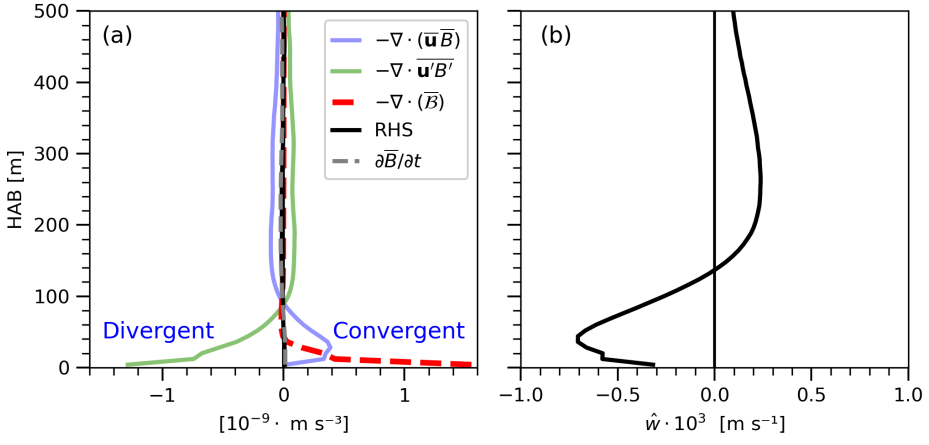

FIG. 4. (a) Tidally averaged buoyancy budget, further averaged over height above bottom (HAB) and across 10 tidal periods (451–461). RHS denotes the sum of the right-hand-side terms in Eq. 7 and is balanced by the buoyancy tendency term, both of which are ~ 0. Positive and negative values indicate convergent and divergent buoyancy fluxes, respectively. (b) Gravity-aligned vertical velocity, averaged similarly as the budget terms. The mean vertical velocity is negative near the bottom, indicating net downwelling.

4. Diapycnal Upwelling

a. Mixing-Driven Upslope Mean Current

To explore the influence of topographic slopes on the mean flow, we examine the mean circulation induced by internal tide-driven mixing in the tilted ($\theta = 0.0036$ rad) and flat ($\theta = 0$) cases. The flow structure is visualized using a streamfunction derived from the y-integrated velocity field,

$$\psi(x,z) = \int_0^y \int_0^{z'=z} -\overline{u}\, dz dy, \tag{11}$$

overlaid with total buoyancy contours and mean velocity arrows, with the mean topographic height delineated by a brown contour (Fig. 5). The velocity fields are averaged over tidal periods 451-461, focusing on the mean flow.

In the tilted case (Fig. 5a), the streamfunction exhibits a pronounced pattern with values generally decreasing in the slope-normal direction, corresponding to a strong upslope mean flow (also evident from the arrows). The upslope transport peaks at the depth of the sill, aligned with steepened buoyancy contours, suggesting a mixing-driven mean flow transporting water upward. Similar strong up-canyon mean flow was found by Drake et al. (2022a), who attributed the layered structure to hydraulic control at the sill. They found that the major topographic sills blocked the along-thalweg transport from restratifying the canyon trough, leading to a continual erosion of stratification below the blocking depth. This upslope current, a hallmark of diapycnal upwelling, supports the observation of a finite near-bottom stratification at equilibrium, consistent with enhanced mixing over sloping topography (Garrett et al. 1993; Drake et al. 2022a). In the flat case (Fig. 5b), the streamfunction is markedly weaker. The arrows show recirculation cells, while buoyancy contours indicate a more uniform, homogenized water column near seafloor. This absence of a coherent upslope current highlights the critical role of the slope in organizing the mean flow and driving diapycnal upwelling, as the flat case lacks the restratification necessary to sustain such circulation (Garrett et al. 1993).

b. Diapycnal upwelling due to mixing-driven water mass transformation

The streamfunction analysis in the previous section demonstrates there is a time-mean Eulerian velocity across time-mean buoyancy surfaces, $\overline{\boldsymbol{u}} \cdot \overline{\boldsymbol{n}_B}$, in the upwelling direction. However, this is

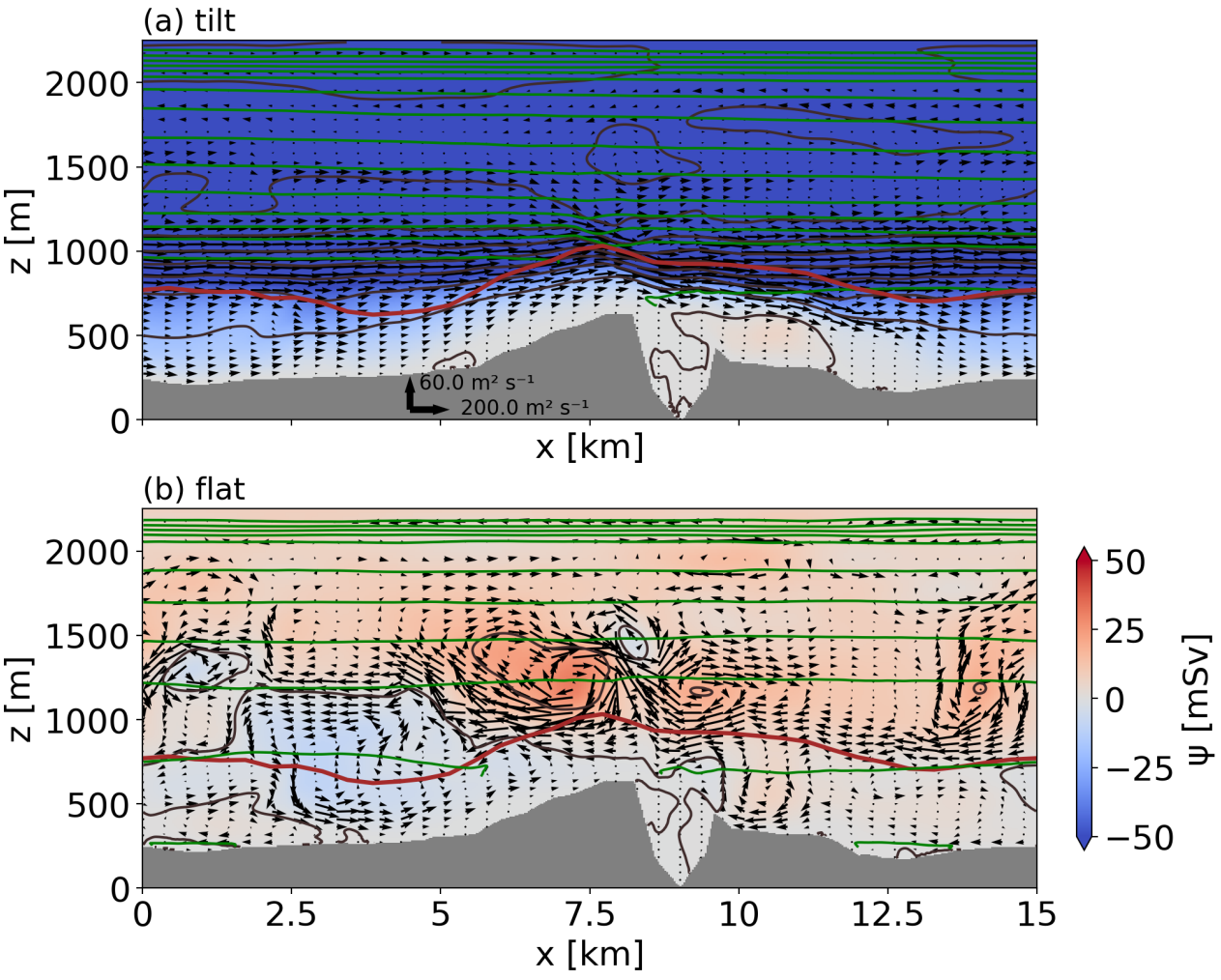

301 FIG. 5. Streamfunction from cross-canyon (y) integrated velocities, averaged over 10 tidal periods (451-461).
302 (a) The slope angle $\theta = 0.0036$ rad, (b) $\theta = 0$. The green contours represent the total buoyancy at the center of
303 the domain ($y = L_y/2$), with an interval of 0.0001. The brown contour represents the y-averaged seafloor depth,
304 for reference. Shaded regions indicate the minimum seafloor depth in the cross-canyon direction.

308 not necessarily the same as the time-mean residual velocity across buoyancy surfaces, $\overline{\boldsymbol{u}\cdot\boldsymbol{n}_B}$. The
309 residual upwelling can be related to the diapycnal velocity induced by water mass transformations
310 by accounting for the instantaneous velocity of isopycnals themselves. When considering the mean
311 slope current, there are three key velocity components to take into account: the Eulerian velocity
312 across isopycnal surfaces (Eulerian diapycnal velocity), the velocity of isopycnal surfaces, and the
313 Lagrangian diapycnal velocity. The Eulerian diapycnal velocity, defined as $(\boldsymbol{u}\cdot\boldsymbol{n}_B)\boldsymbol{n}_B$, represents
314 the component of velocity normal to the buoyancy surfaces. In a quiescent flow ($\boldsymbol{u} = 0$), the Eulerian

diapycnal velocity vanishes but there can still be a non-zero Lagrangian diapycnal velocity due isopycnal surfaces moving through stationary water parcels. Therefore, we need to account for the velocity of an isopycnal surface, $\boldsymbol{u}_B$, which is normal to the isopycnal by construction. Subtracting the Eulerian diapycnal velocity from isopycnal velocity, we get a Lagrangian view of the diapycnal velocity, which is purely related to the irreversible mixing that transforms the water mass. To yield the mathematical expression of this Lagrangian diapycnal velocity, we begin with the Boussinesq buoyancy equation,

$$\frac{\partial B}{\partial t} = -\boldsymbol{u} \cdot \nabla B - \nabla \cdot \mathcal{B}. \tag{12}$$

Assuming there exists an isopycnal velocity $\boldsymbol{u}_B$ that satisfies the kinematic relationship,

$$\frac{\partial B}{\partial t} + \boldsymbol{u}_B \cdot \nabla B = 0, \tag{13}$$

the isopycnal velocity is then

$$\boldsymbol{u}_B = -\frac{1}{|\nabla B|} \frac{\partial B}{\partial t} \boldsymbol{n}_b. \tag{14}$$

Dividing Eq. (12) by the buoyancy gradient magnitude $|\nabla B|$, multiplying by $\boldsymbol{n}_B$, and substituting in expression in Eq. (14), we get the Lagrangian diapycnal velocity (Marshall et al. 1999),

$$\boldsymbol{e} \equiv (\boldsymbol{u} \cdot \boldsymbol{n}_B)\, \boldsymbol{n}_B - \boldsymbol{u}_B = -\frac{\nabla \cdot \mathcal{B}}{|\nabla B|} \boldsymbol{n}_B. \tag{15}$$

Since the buoyancy field has reached a quasi-equilibrium state, we assume that $\overline{\boldsymbol{u}_B}$ is negligible, implying that the time-mean diffusive buoyancy flux convergence provides a reasonable estimate of the residual mean transport across buoyancy surfaces:

$$\overline{(\boldsymbol{u} \cdot \boldsymbol{n}_B)} \simeq -\frac{\overline{\nabla \cdot \mathcal{B}}}{|\nabla B|}. \tag{16}$$

This approximation provides the connection that allows the diapycnal transport diagnosed from the water-mass transformation (WMT) framework to be meaningfully interpreted as the time-mean cross-isopycnal transport in the quasi-steady regime.

To get the transport due to diapycnal mixing, we integrate the diapycnal velocity [Eq. (16)] across a buoyancy surface $\mathcal{A}(B,t)$,

$$\mathcal{E}(B,t) = \iint_{\mathcal{A}(B,t)} \boldsymbol{e}\cdot\boldsymbol{n}_B \, d\mathcal{S} = -\iint_{\mathcal{A}(B,t)} \frac{\nabla\cdot\mathcal{B}}{|\nabla B|}\, d\mathcal{S}. \tag{17}$$

Evaluating the expressions in Eq. (17) is challenging because it involves interpolating fields onto a highly-variable buoyancy surfaces; a more convenient approach is to re-express the right-hand-side into a volume integral (Marshall et al. 1999). Suppose dh represents a small distance between two isopycnals $d\mathcal{S}$ represents a small surface area element tangent to these isopycnals. Then, the corresponding small volume element between the isopycnals can be expressed in buoyancy coordinates as (Drake et al. 2025)

$$d\mathcal{V} = dh d\mathcal{S} = \frac{dB}{|\nabla B|} d\mathcal{S}. \tag{18}$$

Therefore, Eq. (17) can be expressed as,

$$\mathcal{E}(B,t) \equiv -\frac{\partial}{\partial B} \iiint_{\mathcal{V}_{\leq}(B,t)} \nabla\cdot\mathcal{B}\, d\mathcal{V}, \tag{19}$$

where $\mathcal{V}_{\leq}(B,t) \equiv \{\boldsymbol{x} \,|B'(\boldsymbol{x},t) \leq B\}$ is the volume enclosing any water less buoyant than B.

To quantify the water mass transformation rate ($\mathcal{E}$) driven by diapycnal mixing, we approximate the volume-integrated diapycnal flux divergence by finite difference, evaluating the integrand of Eq. (19) for discrete buoyancy layers. For each buoyancy bin of width $\delta B = 2\times10^{-5}$ m s^{-2}, we compute the control volume, $\delta\mathcal{V}(B,t) = \mathcal{V}(B+\delta B/2,t) \cap \mathcal{V}(B-\delta B/2,t)$. Evaluating this integral requires tracing buoyancy surfaces from the bottom boundary to the upper boundary. To ensure a fully enclosed volume, the simulation domain is periodically extended by stitching 40 copies in the cross-slope direction (Fig. 6a, green lines; Drake et al. 2022b).

For intuitive interpretation, we express the transformation rate as a function of buoyancy and height above the bottom (HAB), denoted as $\delta\mathcal{E}(\mathrm{HAB},B,t)$ (Holmes and McDougall 2020). Analogous to the geometric derivation of Holmes and McDougall (2020), $\delta\mathcal{E}$ is defined by considering the flux convergence within an infinitesimal region, $\delta\mathcal{V}(\mathrm{HAB},B,t)$, bounded by two buoyancy surfaces and two HAB interfaces (blue shaded region in Fig. 6a):

$$\delta\mathcal{E}(\mathrm{HAB},B,t) = -\frac{1}{\delta B}\iiint_{\delta\mathcal{V}(\mathrm{HAB},B,t)} \nabla\cdot\mathcal{B}\; d\mathcal{V}, \tag{20}$$

The total buoyancy transformation rate is recovered by integrating $\delta\mathcal{E}$ vertically across all HAB,

$$\mathcal{E}(B,t) = \int_0^\infty \frac{\delta\mathcal{E}(\mathrm{HAB},B,t)}{\delta\mathrm{HAB}}\; d\mathrm{HAB}. \tag{21}$$

Analysis of the mean transformations shows that the most intense diapycnal upwelling occurs within a 40 m thick Bottom Boundary Layer (BBL), defined as the bottom layer over which the mixing-driven watermass transformation is positive (Fig. 6b). Above this layer, a 40-200 m thick Stratified Mixing Layer (SML) exhibits diapycnal downwelling, with transport magnitudes much smaller than the upwelling in the BBL. The total diapycnal upwelling transport averaged over buoyancy in the BBL, $\sum_{\mathrm{HAB}}\langle\delta\mathcal{E}_{BBL}\rangle_B$, and the corresponding downwelling transport in the SML, $\sum_{\mathrm{HAB}}\langle\delta\mathcal{E}_{SML}\rangle_B$, are approximately 150 mSv and -10 mSv, respectively—values with the same orders of magnitude as observational estimates in fracture zone canyons (Thurnherr et al. 2020). Although these estimates pertain to a single abyssal sloping canyon, similar bottom-intensified upwelling is expected to occur across numerous abyssal hills and canyons globally. When integrated over the global seafloor, such localized diapycnal upwelling could represent a significant contribution to the deep branch of the global overturning circulation.

5. Lagrangian Particle Tracking and Tracer Evolution

To elucidate the transport and mixing dynamics driven by internal tides in the Brazil Basin's fracture zone canyon, we released 5×10^5 Lagrangian particles and an inert passive tracer. The initial conditions of the particles were randomly sampled from the probability distribution $\mathcal{P}_0$ that is proportional to the initial tracer concentration C_0, enabling direct comparisons. Both follow a 3D Gaussian profile, centered at $\hat{x}_0 = \hat{L}_x/4$, $y_0 = L_y/2$, and $\hat{z}_0 = 1000$ m, defined as:

$$\mathcal{P}_0(\hat{x},y,\hat{z}) = C_0(\hat{x},y,\hat{z}) = -\exp\left[\frac{(\hat{x}-\hat{x}_0)^2}{2\sigma_{\hat{x}}^2} + \frac{(y-y_0)^2}{2\sigma_y^2} + \frac{(\hat{z}-\hat{z}_0)^2}{2\sigma_{\hat{z}}^2}\right], \tag{22}$$

where $\sigma_{\hat{x}} = \sigma_y = 1000$ m and $\sigma_{\hat{z}} = 50$ m. Although our objective is to investigate near-bottom processes, the particles are initialized 1000 m above the mean slope rather than directly at the

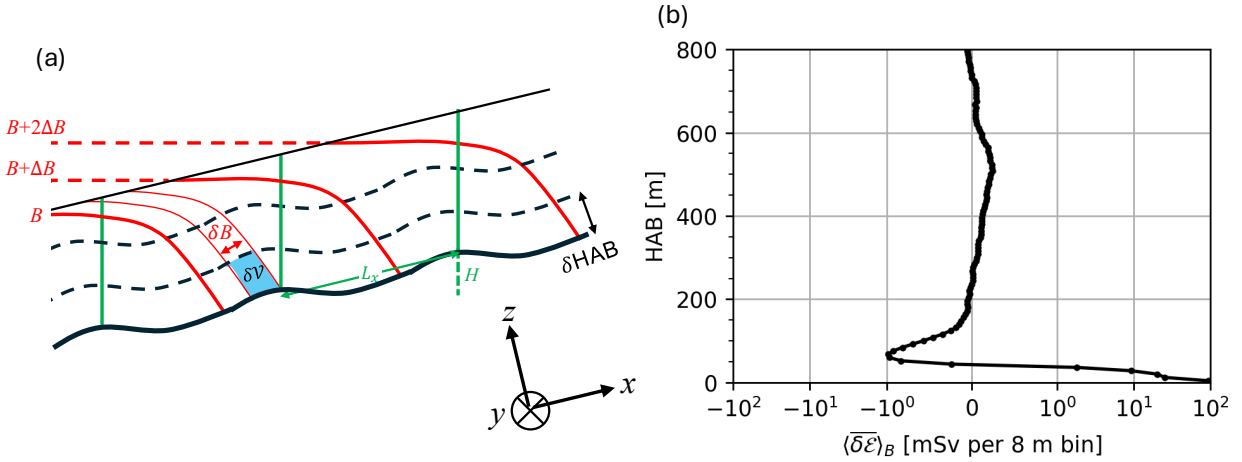

FIG. 6. (a) Schematic of water mass transformation due to turbulent mixing. To capture the water mass, multiple copies of the model domain are required to enclose the water mass. The mean slope θ is greatly exaggerated in this schematic for clarity; while only 3 copies of the domain appear to be required to close enclose the water masses bounded by two isopycnals in this schematic, our analysis requires 40 copies. ΔB is defined as $N^2 H$, where $H = L_x \sin\theta$. The water mass is binned such that it depends on buoyancy and HAB. (b) $\delta\mathcal{E}$, averaged over 10 tidal periods and over the range of buoyancies ΔB that cover the domain, and in terms of 8 m HAB bins.

seafloor. This placement ensures that the particle cloud is advected across the central sill by the Eulerian upslope mean flow (Fig. 5a), thereby bringing a large fraction of the particles into close proximity with the bottom. By contrast, particles released directly at the bottom would be less likely to cross the sill and could remain trapped locally in weakly-stratified depressions, limiting their ability to sample the key dynamics of interest. To avoid an overly broad buoyancy distribution, particles and tracers are initialized anisotropically in the gravity-aligned system.

a. Lagrangian particle tracking

The Lagrangian particles follow the resolved flow $\boldsymbol{u}$ without the inclusion of Brownian motion due to subgrid scale diffusion, i.e. their positions evolve according to

$$\boldsymbol{X}^p(t) = \boldsymbol{X}_0^p + \int_{t_0}^{t} \boldsymbol{u}\, dt, \tag{23}$$

where $\boldsymbol{X}_0^p$ denotes the unique initial position of particle p and t_0 is the release time.

This Lagrangian particle-tracking framework offers a powerful diagnostic advantage for simulations with periodic boundaries, as particles that cross the periodic boundaries can be continuously tracked in an extended, virtual domain. Specifically, when particles cross one of the periodic boundaries, their positions are incremented by the length of the domain in that direction. To account for the background stratification, we additionally increment each particle's total buoyancy by $\pm\Delta B$ when they cross the periodic boundary in the cross-slope direction. This technique effectively reconstructs long-range transport without the added computational cost of simulating a physically larger model domain, thus enabling a more complete and uninterrupted view of particle dispersion and transport pathways.

A snapshot of the particles over ten tidal cycles after release ($t_f = 461$ tidal periods) in the tilted configuration reveals an extended domain in which a large fraction of particles migrate upslope toward the east, while a subset is advected northward through the channel. The particle trajectories are strongly influenced by the sill, where many particles plunge sharply before being redistributed by the oscillatory flow (Fig. 7). The color shows the buoyancy deviation from the initial release at t_0, defined as $\Delta B^p(t_f) = B^p(t_f) - B^p(t_0)$. A time-evolving visualization of these trajectories is provided in a supplementary movie S2.

We further examine the temporal evolution of particle buoyancy by classifying them into two groups: particles with increased buoyancy [$\Delta B^p(t_f) > 0$] and those with decreased buoyancy [$\Delta B^p(t_f) < 0$]. A similar classification is applied to the vertical position change, $\Delta\hat{Z}^p(t_f)$, separating particles that ascend [$\Delta\hat{Z}^p(t_f) > 0$] from those that descend [$\Delta\hat{Z}^p(t_f) < 0$].

The probability density functions (PDFs) of both buoyancy and vertical displacement broaden over time, with a distinct mean shift toward positive values (Fig. 8a,b). Median trends for all particles and for the buoyancy-increased and buoyancy-decreased subsets show that, on average, particle buoyancy and elevation both increase with time. While a large fraction of particles gain buoyancy and rise (green), a smaller yet comparable portion undergoes buoyancy and elevation decreases (orange). Tidal oscillation is evident in the particle vertical position $\hat{Z}^p$ but not in buoyancy $\hat{B}^p$. This contrast arises because $\hat{Z}^p$ responds to adiabatic, reversible internal wave motions that vertically displace parcels without changing their buoyancy. In contrast, $\hat{B}^p$ reflects irreversible diabatic processes, such as turbulent mixing, that modify a parcel's intrinsic buoyancy.

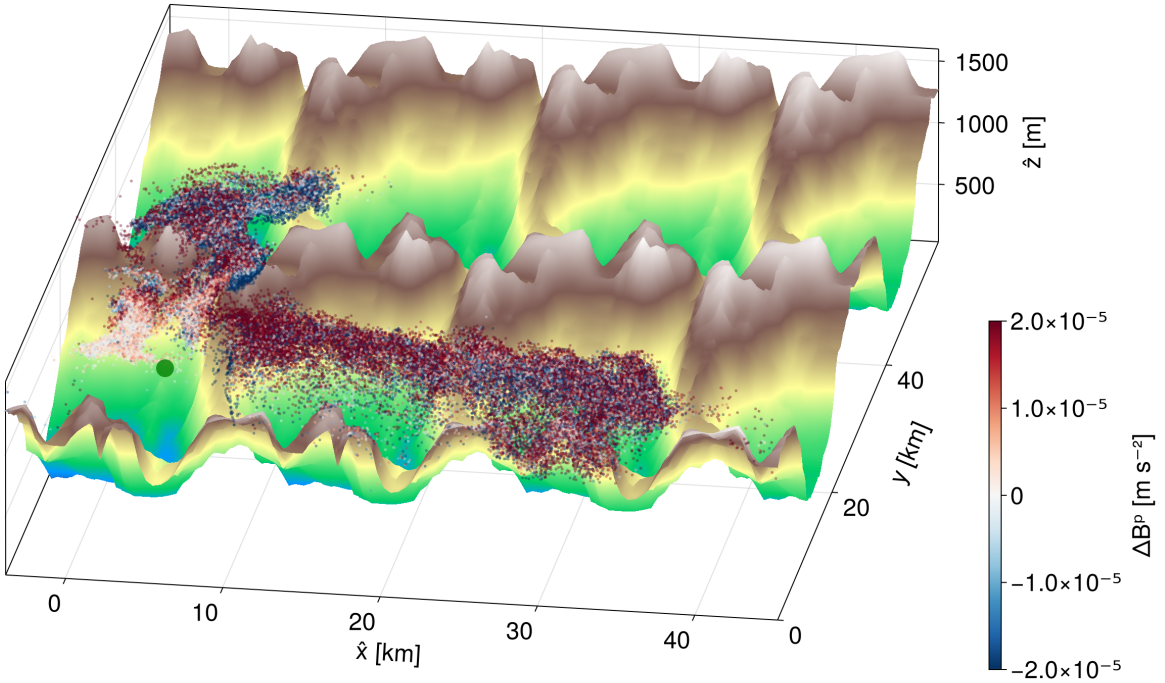

FIG. 7. Three dimensional snapshot of the particle spatial distribution with buoyancy difference [$\Delta B^p(t_f) = B^p(t_f) - B^p(t_0)$] as color. Two distinct groups: one travels upslope (positive $\hat{x}$), and one travels through the northern channel. The green dot shows the center location of the particles at release point. Multiple copies of the domain are evident from the repeated pattern of topographic roughness that is added on top of the mean slope.

Therefore, particle buoyancy change serves as a more direct and robust indicator of diapycnal upwelling than vertical displacement (Wynne-Cattanach et al. 2024).

The ratio between the number of particles with increasing and decreasing buoyancy, $N^p_{B_+}(t)/N^p_{B_-}(t)$, rises steadily and approaches a value of about two after eleven tidal cycles (Fig. 8c), suggesting that buoyancy gains dominate overall. In contrast, the ratio of ascending to descending particles, $N^p_{Z_+}(t)/N^p_{Z_-}(t)$, exhibits strong oscillations early on (Fig. 8d), reflecting particles that temporarily rise before crossing the sill and subsequently descend. These fluctuations dampen over time, but the ratio remains above unity, indicating a persistent preference for upward motion associated with upslope mixing.

At the final time (t_f), the particle ensemble separates into two distinct spatial groups: one located upstream of the first sill or within the northern channel [$\hat{X}^p(t_f) < 15$ km], and another that has crossed the sill and continues upslope toward the subsequent sills [$\hat{X}^p(t_f) > 15$ km]. In the upstream region, buoyancy changes $\hat{B}^p(t_f)$ are positively correlated with vertical displacements $\hat{Z}^p(t_f)$, consistent with physical intuition—particles that become more buoyant also move upward (Fig. 8e). Most of these particles undergo small oscillations in both buoyancy and elevation, reflecting tidal motions that are largely adiabatic and confined within the canyon (see the white cluster in Fig. 7).

Downstream of the sill, the relationship between ΔB^p and $\Delta\hat{Z}^p$ becomes more complex (Fig. 8f). The joint PDF exhibits two distinct signatures: (1) a weakly correlated, nearly symmetric core centered around $\Delta B^p \approx 0$, representing particles undergoing hydraulically controlled overflow that descend substantially ($\Delta\hat{Z}^p < 0$) while remaining nearly adiabatic (constant B^p); and (2) an asymmetric tail in the first quadrant ($\Delta B^p > 0$, $\Delta\hat{Z}^p > 0$), indicating irreversible buoyancy increases due to turbulent diapycnal upwelling.

This interpretation is supported by the spatial variation of the correlation coefficient $r_{\Delta B^p, \Delta\hat{Z}^p}$ (Fig. 9). Correlation peaks sharply near the sill ($\hat{x} \sim 8, 22,$ and 37 km), where strong turbulence and enhanced mixing generate significant diapycnal buoyancy fluxes. Immediately downstream of each sill, $r_{\Delta B^p, \Delta\hat{Z}^p}$ drops, consistent with overflow that is predominantly adiabatic. In other words, mixing-induced upwelling dominates upstream and at the sill crest, while the flow downstream is governed by hydraulically controlled descent along isopycnals. Together, these results suggest that both processes—localized turbulent mixing and adiabatic overflow—jointly shape the vertical and buoyancy evolution of particles near the sill. The strong correlation between ΔB^p and $\Delta\hat{Z}^p$ near the sill provides Lagrangian evidence of where turbulent mixing converts mechanical energy into irreversible buoyancy flux.

The correlation coefficient between buoyancy change and vertical displacement, $r_{\Delta B^p, \Delta\hat{Z}^p}$ as a function of $\hat{x}$ shows that at t_f, correlation is large for particles near the first sill $\hat{x} < 8$ km but reduces drastically for particles further upslope away from the first sill (Fig. 9). In addition, $r_{\Delta B^p, \Delta\hat{Z}^p}$ tends to increase as particles approach the sill, but decreases sharply at the right side of each sills, corresponding to the left symmetric tail of Fig. 8f. This is a strong indicator that

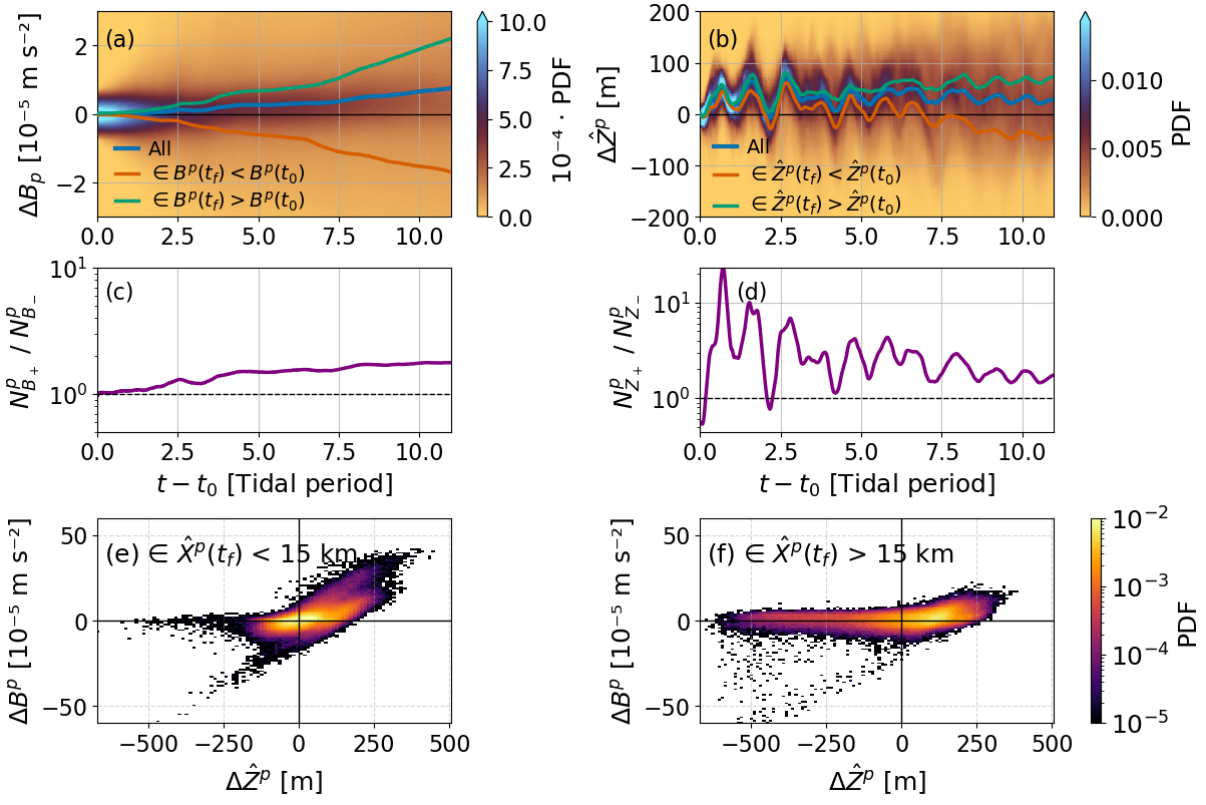

458 FIG. 8. (a) Probability density function (PDF) of buoyancy change, $\Delta B^p = B^p(t) - B^p(t_0)$, where t_0 is the
459 initial release time. Median values are shown for all particles (blue), particles with decreased buoyancy at the
460 final time ($B^p(t_f) < B^p(t_0)$, orange), and particles with increased buoyancy ($B^p(t_f) > B^p(t_0)$, green). (b)
461 Same as (a), but for vertical displacement, $\Delta \hat{Z}^p = \hat{Z}^p(t) - \hat{Z}^p(t_0)$. (c,d) Time evolution of the ratio between the
462 number of particles with increasing and decreasing (c) buoyancy and (d) vertical position, relative to their values
463 at t_0. In contrast to panels (a,b), where particle groups are classified based on changes between t_f and t_0, the
464 classifications in (c,d) are updated dynamically at each time step to reflect instantaneous trends. (e,f) Joint PDFs
465 of buoyancy change and vertical displacement at the final time t_f, for particles located (e) upslope $\hat{X}^p(t_f) < 15$
466 km and (f) upslope $\hat{X}^p(t_f) > 15$ km.

472 turbulent mixing occurs near the sill creating diapycnal upwelling, but hydraulically-controlled
473 overflow brings particles downward without changing buoyancy.

476 To identify where these buoyancy changes occur, we compute the mean net buoyancy rate of
477 change for each (x, y) spatial bin,

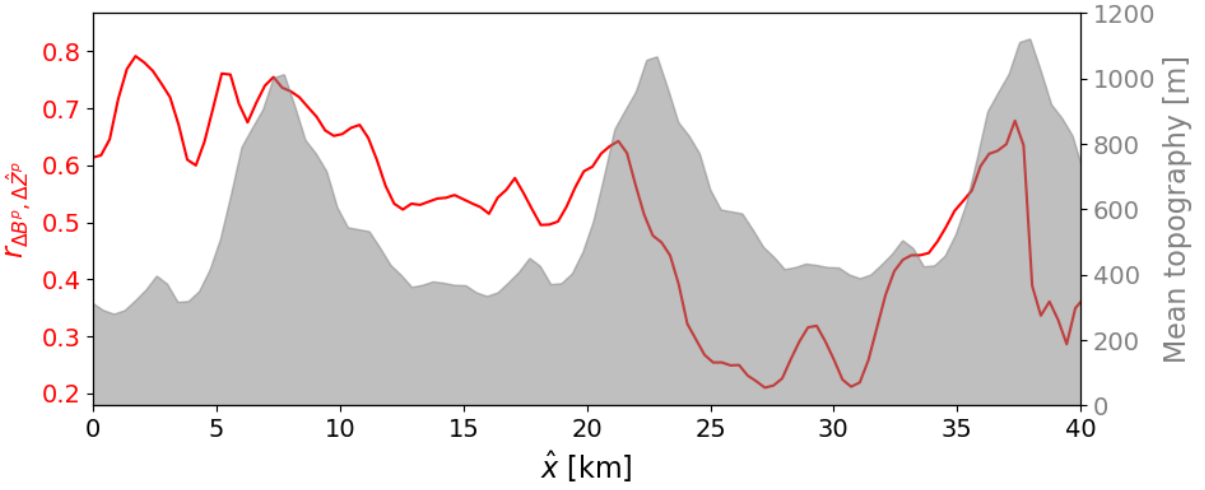

FIG. 9. Ensemble averaged correlation coefficient of particle buoyancy change ΔB^p and $\Delta \hat{Z}^p$, superimposed with the mean topography (average over $y = L_y/3$ to $2L_y/3$ at final timestep.

$$\overline{\omega}^p(x,y) = \frac{\sum_t \sum_{\forall \hat{\boldsymbol{X}}^p(t) \in \text{bin}} \frac{dB^p}{dt}}{\sum_t \sum_{\forall \hat{\boldsymbol{X}}^p(t) \in \text{bin}}}, \tag{24}$$

and map its distribution over ten tidal cycles (Fig. 10).

Regions of pronounced buoyancy change coincide with major topographic features—particularly near the sills (with a first copy at $\hat{x} \approx 8$ km and a second at 23 km) and within the northwestern channel. For example, particles in the buoyancy-decreased group display negative mean buoyancy change ($\bar{\omega}^p$, blue, Fig. 10b) near the sill, whereas those in the buoyancy-increased group exhibit positive $\bar{\omega}^p$ (red, Fig. 10c) along the same structures. This spatial alignment indicates that topography modulates the local balance between downwelling and upwelling transport. The comparison between the two particle groups reveals that buoyancy gains exceed buoyancy losses, implying a net diapycnal upwelling effect. This asymmetry highlights the central role of abyssal topography in promoting irreversible water-mass transformation.

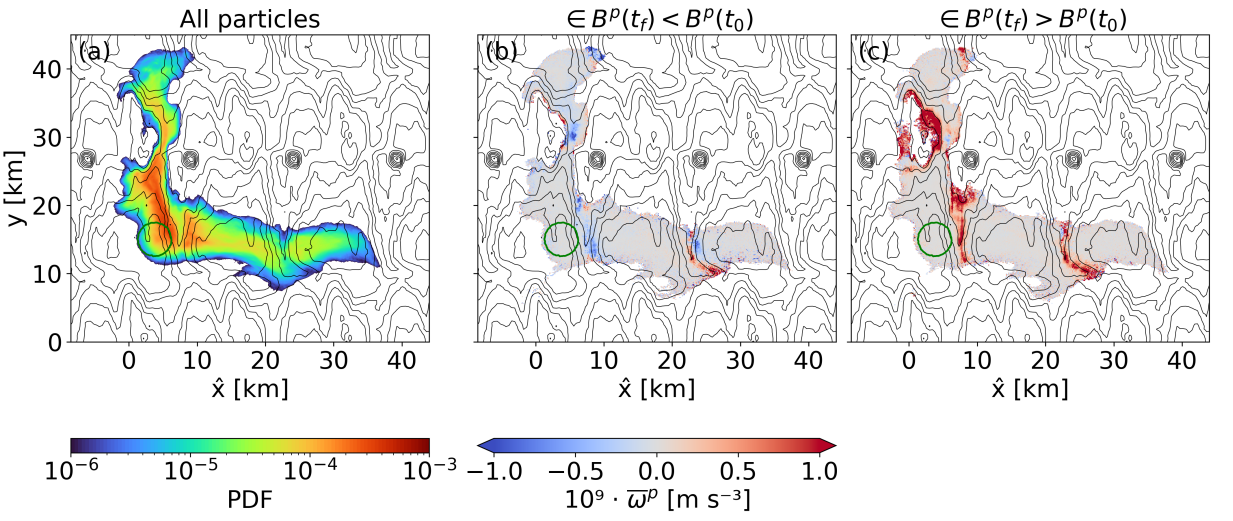

488 FIG. 10. Spatial distribution and buoyancy changes of Lagrangian particles over ten M_2 tidal cycles. Panels (a,
489 d, g) show the probability density function (PDF) of all particles, particles with increased buoyancy ($B^p(t_f) >$
490 $B^p(t_0)$), and particles with decreased buoyancy ($B^p(t_f) < B^p(t_0)$), respectively, where t_0 is the release time and
491 t_f is ten tidal periods later. Panels (b, c) show the mean buoyancy tendency $\overline{\omega}^p$ for buoyancy-decreased and
492 buoyancy-increased particles, respectively.

493 *b. Tracer-weighted buoyancy*

494 To capture the effects of turbulent diffusion that the Lagrangian particles inherently lack, we addi-
495 tionally follow an analogously-released passive tracer. The tracer evolution offers a complementary
496 Lagrangian measure of diapycnal upwelling, evaluated using the tracer-weighted buoyancy, $\overline{B}^c$,
497 where the tracer-weighted average is defined as

$$\overline{(\cdot)}^c = \frac{\iiint (\cdot)\, c \, dxdydz}{\iiint c \, dxdydz}. \tag{25}$$

498 Ruan and Ferrari (2021) derive the remarkable exact result that the tracer-weighted average buoy-
499 ancy evolves according to twice the tracer-weighted average diffusive buoyancy flux convergence,

$$\frac{d\overline{B}^c}{dt} = 2\overline{\omega}^c, \tag{26}$$

where $\omega \equiv -\nabla \cdot \mathcal{B}$. The factor of two arises because the turbulent diffusivity induces two distinct effects: turbulent buoyancy fluxes induce a diapycnal velocity, which advects the tracer across buoyancy surfaces, and turbulent diffusive fluxes directly transport tracer across buoyancy surfaces. Integrating Eq. (26) over time gives,

$$\Delta\overline{B}^{c}(t) \equiv \overline{B}^{c}(t) - \overline{B}^{c}(t_0) = \int_{t_0}^{t} 2\overline{\omega}^{c}\, dt. \tag{27}$$

Unlike the Lagrangian particles, whose position and hence total buoyancy can be incremented as they cross the periodic cross-slope (x) boundary, the tracer total buoyancy becomes ambiguous when it spreads across the boundary, making it impossible to evaluate the LHS of Eq. (27). We sidestep this limitation by instead evaluating the RHS of Eq. (27), which only involves gradients of the background buoyancy and hence is unaffected by the tracer crossing the cross-slope boundary.

Notable differences emerge between the tilted and flat cases (Fig. 11). In the tilted case ($\theta = 0.0036$), both the tracer-weighted average buoyancy difference $\Delta\overline{B}^{c}_{\text{tilt}}$ and the mean particles buoyancy difference $\Delta\overline{B}^{p}_{\text{tilt}}$ increase with time, indicating enhanced mixing and diapyncal upwelling. Two sets of particle releases at different times (p1 and p2) show different evolution but a similar trend, reflecting the stochastic and intermittent nature of turbulent transport. The tracer-weighted buoyancy increase, however, is roughly twice that of the particles after four tidal cycles. This discrepancy arises because in our setup, Lagrangian particles are purely advective and do not experience subgrid turbulent diffusion or Brownian motion. In reality, turbulent diffusion acts as a random walk superimposed on the mean flow, allowing fluid parcels to experience small-scale mixing events that redistribute buoyancy irreversibly. The absence of this stochastic component means that particles only sample the resolved advection field, whereas tracers evolve diffusively under the LES closure. As a result, $\Delta\overline{B}^{c}$, which reflects the covariance between buoyancy and tracer concentration (see Ruan and Ferrari 2021), evolves at a rate of approximately twice that of the particles.

In contrast, for the flat-bottom case, both $\Delta\overline{B}^{c}_{\text{flat}}$ and $\Delta\overline{B}^{p}_{\text{flat}}$ remain nearly constant, reflecting weak stratification and minimal buoyancy flux within the thick, homogenized mixing layer. These results confirm that enhanced buoyancy evolution and diapycnal upwelling critically depend on the presence of a sloping boundary.

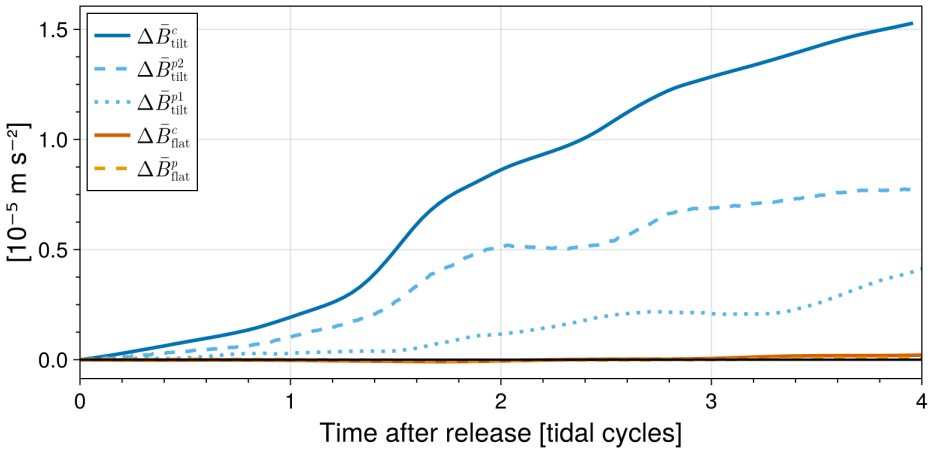

FIG. 11. Evolution of tracer-weighted buoyancy change (solid lines) and the mean buoyancy change of Lagrangian particles (dotted and dashed lines) for the tilted and flat cases. Two particle releases are performed in the tilted case to illustrate stochastic variability in particle evolution: set p1 at $t = 451$ and set p2 at $t = 458$ tidal periods. The tracer is released concurrently with p2, representing the same water mass as the second particle set. The flat-bottom case includes both tracer and particle releases at $t = 451$ tidal period. Despite the different release times, all experiments consistently show an increase in buoyancy, confirming robust diapycnal upwelling in the tilted configuration.

6. Discussion and Conclusion

Tidally-driven mixing plays a fundamental role in maintaining the global overturning circulation and shaping abyssal stratification. However, our understanding of how tidally generated turbulence interacts with topographic slopes to drive diapycnal exchange remains incomplete. In particular, little is known of the interactions between tidally-driven turbulent mixing and the mean overturning circulations that they induce. Here, we employ large-eddy simulations (LES) to force the model with only a barotropic M_2 tide body force, allowing internal waves, instabilities, turbulence, and mean flows to emerge naturally.

The conceptual framework of an "upside down" abyssal circulation, proposed by Ferrari et al. (2016), envisions diapycnal upwelling driven by turbulent mixing along sloping boundaries. In this picture, a parcel of water situated just above the seabed experiences a convergent buoyancy flux: turbulent diffusion transports lighter water downward, and in the absence of a buoyancy flux through the boundary, the near-bottom parcel becomes lighter and rises—producing a net diapycnal

upwelling. Building on this framework, Drake et al. (2022a) examined sloping canyon dynamics where baroclinic instabilities and diffusive fluxes jointly create a convergent buoyancy transport balanced by a divergent mean buoyancy flux associated with an upslope mean flow (Fig. 12a). Our results extend this framework to a tidally dominated regime (without an evident baroclinic eddy flux), revealing a contrasting balance that highlights the role of high-frequency tidal processes in shaping abyssal buoyancy structure. The sloping bottom enables a balance of three primary fluxes: a convergent subgrid-scale (SGS) diffusive flux, a convergent subtidal mean flux, and a divergent tidal eddy flux that counteracts both (Fig. 12b).

The height-above-bottom structure of each term in the buoyancy budget provides insight into how stratification is maintained against near-bottom mixing. Drake et al. (2022a) emphasize a re-stratification mechanism driven by submesoscale baroclinic eddies that act against mixing-induced destratification. Our results show that the vertical gradients of the buoyancy budget terms are instead dominated by high-frequency tidal eddy fluxes: the bottom-enhanced nature of their divergence (buoyancy loss) acts to restore the vertical buoyancy gradient eroded by turbulent diffusion. This finding underscores a new pathway for restratification in tidally energetic environments, where high-frequency eddies, rather than submesoscale baroclinic eddies (Drake et al. 2022a), sustain vertical stratification against turbulent diffusive mixing. Understanding the coupling between tidal eddy restratification and subtidal downwelling remains an open question, central to closing the abyssal buoyancy and overturning budgets. However, the details of how tidal eddy motions and subtidal downwelling interact remain unexplored and warrant further investigation.

The sloping topography also enables the development of a persistent upslope mean current, a feature absent in the flat-bottom case. This upslope mean flow arises from the diapycnal upwelling, modified by hydraulic control by the blocking sill, where the flow is intensified (Drake et al. 2022a). Because the robust upslope flow in the tilted case crosses buoyancy surfaces, it corresponds to the mean diapycnal upwelling required to close the global overturning circulation (Thurnherr et al. 2020), a process absent in the flat-bottom scenario. Although the time-mean bottom vertical velocity appears negative on average (Fig. 4b), this does not contradict the presence of an upslope mean flow. The apparent discrepancy arises because the cross-canyon (y) integration blends localized downwelling at the sill and near the flanks with more widespread upslope transport within the canyon, effectively obscuring the spatial structure of the flow. Our results align with

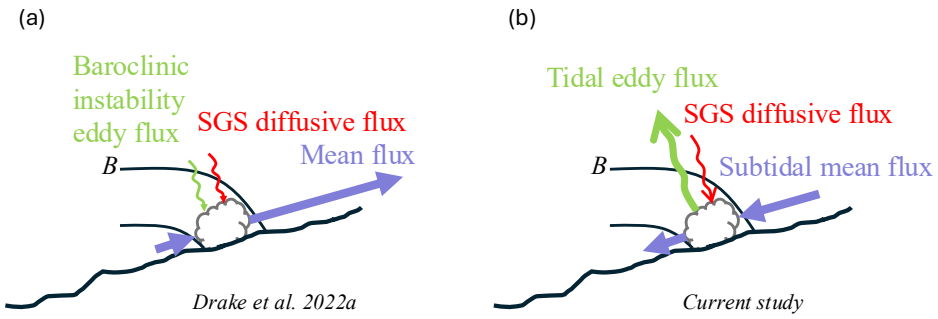

FIG. 12. Schematic illustration of buoyancy flux balances along a sloping seafloor. (a) Conceptual framework adapted from Drake et al. (2022a), where the subgrid-scale (SGS) diffusive flux (red curly arrow) and the baroclinic eddy flux (green curly arrow) converge and are balanced by a divergent mean transport. (b) Framework from this study, in which the SGS diffusive flux and convergent mean transport are balanced by a divergent tidal eddy flux. Contours are buoyancy. Arrows are schematic and do not indicate the precise flux directions.

theoretical and observational evidence, emphasizing the interplay between topography and mixing in shaping ocean circulation (Thurnherr et al. 2020; Drake et al. 2022a). A substantial water-mass transformation occurs within the bottom boundary layer and drives approximately 150 Sv of diapycnal upwelling when integrated across the domain. Although this value represents only one sloping canyon, it suggests that slope-induced tidal processes could contribute significantly to the global abyssal circulation when integrated over many such topographic features worldwide.

Motivated by tracer release experiments in the ocean (e.g. Ledwell et al. 1998; Watson et al. 2013; Wynne-Cattanach et al. 2024) and by numerical studies employing passive tracers to quantify diapycnal exchange (e.g. Drake et al. 2022b), we released a patch of passive tracer a few hundred meters above the topography, complemented by an equivalent cloud of Lagrangian particles. The Lagrangian diagnostics reveal that, on average, the particles not only gain buoyancy but also undergo persistent upward displacements, demonstrating that mixing in the presence of a slope drives diapycnal upwelling and a corresponding up-hill Lagrangian transport. Near the sill crest, changes in particle buoyancy correlate strongly with vertical displacement, whereas over the sill, particles descend due to the hydraulically-controlled overflow with minor change in buoyancy. In the simulation with a sloping bottom, the tracer-weighted mean buoyancy increases steadily over time, whereas it remains nearly constant in the flat-bottom case, underscoring the

profound influence of topographic slope on vertical mass exchange. This Lagrangian perspective provides spatial and temporal localization of where mixing most effectively modifies buoyancy, offering insight into the diapycnal exchanges that cannot be directly inferred from Eulerian averages alone. Extending the Lagrangian particle framework to include stochastic Brownian motion will allow the representation of unresolved turbulent fluctuations and thereby capture realistic particle dispersion. This improvement will enable direct estimation of both Lagrangian and diapycnal diffusivities, facilitating rigorous evaluation of classical dispersion theories (e.g., Taylor 1922; Lien and D'Asaro 2004) in tidally forced, stratified flows. Such advancements will help bridge the gap between numerical simulations and observational estimates of deep-ocean mixing.

Beyond the classical paradigm of diapycnal upwelling along abyssal slopes, recent work has revealed a contrasting yet complementary picture of abyssal dynamics. Much of the global deep ocean exhibits prograde along-slope flows (with positive topostrophy, i.e. in the direction of Kelvin wave propagation), associated with downslope mean flows maintained by mesoscale eddy fluxes and topographic interactions (Capó et al. 2024; Schubert et al. 2024). How such downwelling coexists and interacts with the diapycnal upwelling and restratification processes identified in this study remains an open question of broad significance. In our simulation, a pronounced downhill mean flow emerges despite the absence of mesoscale eddies and topostrophic mean flows. This downward motion appears to arise from tidal rectification, where oscillatory tidal flows generate alternating downwelling jets over supercritical slopes (Sarkar and Scotti 2017), resulting in a rectified mean downslope current (as observed in Lam et al. 2004). These mechanisms differ fundamentally from the mesoscale-eddy driven topostrophic downwelling, yet they may play a comparable role in shaping abyssal exchange. Reconciling tidally-driven upwelling and downwelling within the bottom boundary layer will be essential for understanding abyssal overturning circulation and the maintenance of deep stratification. A companion study will further investigate the dynamics and variability of slope-driven downwelling under tidally dominated conditions.

Acknowledgments. The authors acknowledge the National Science Foundation (NSF) ACCESS program for providing computational resources through allocations on the Delta supercomputer at the National Center for Supercomputing Applications (NCSA). C. -L. L and H. F. D. also acknowledge support from UC Irvine's School of Physical Sciences.

Data availability statement. All the simulation setup and postprocessing files can be found in https://github.com/liuchihl/internal-tide-mixing.

APPENDIX

Grid resolution vs. Ozmidov length scale

A key requirement for accurately representing stratified turbulence in large-eddy simulation (LES) is that the grid spacing be comparable to or smaller than the Ozmidov length scale, L_O. The Ozmidov scale marks the transition between buoyancy-influenced, anisotropic motions and the smallest turbulent eddies that remain isotropic; resolving scales at or below L_O ensures that the turbulent closure is only being applied for represented three-dimensional turbulence, as intended. Strong stratification suppresses vertical motions much more than horizontal ones, making the vertical direction the strictest resolution requirement for capturing overturns and mixing (Ivey et al. 2008). Our horizontal grid spacing (30 m) is roughly four times larger than the minimum vertical spacing, making the grid inherently anisotropic; however, it is the vertical grid spacing that most determines whether turbulence near the Ozmidov scale is resolved.

To assess whether our vertical grid resolution adequately resolves stratified turbulence, we compare the grid spacing with L_O, estimated both pointwise and following the bulk formulation of Khani (2018). This comparison is important because large eddy simulations of stratified turbulence are expected to yield physically consistent results when the grid spacing is comparable to or smaller than L_O (Khani 2018). Following Khani (2018), the bulk Ozmidov length scale is defined as

$$\overline{L_O} = 2\pi \left(\frac{\overline{\varepsilon}}{\overline{N}^3} \right)^{1/2}, \tag{A1}$$

where overbars denote volume averages within turbulent regions, identified as those with $\varepsilon > 10^{-10}$ W kg. In addition, we compute pointwise values $L_O(x, y, z)$ across all turbulent regions. The probability density function shows that our vertical grid spacing is less than most of the

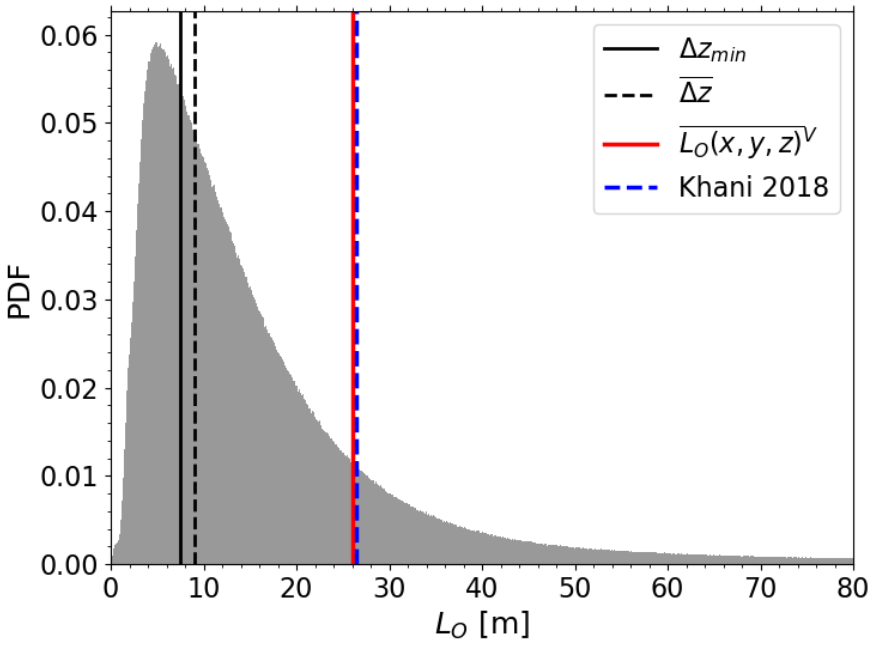

FIG. A1. Probability density function (PDF) of the Ozmidov length scale, L_O, estimated pointwise within turbulent regions ($\varepsilon > 10^{-10}$ W kg^{-1}). The solid and dashed black lines denote the minimum and mean vertical grid spacing, respectively, while the solid red line marks the mean L_O. The dashed blue line corresponds to the reference definition of Khani (2018). Note that the L_O axis is truncated at 80 m for clarity; larger values occur but are not shown for presentation purposes.

estimated L_O values (Fig. A1). The volume-averaged local L_O agrees closely with the bulk value estimated in Eq. A1, corresponding to approximately 3.6 times the minimum vertical grid spacing (Δz_{min}). This suggests that the simulation adequately resolves the dominant turbulent flows in stratified regions, but only marginally so.

References

Callies, J., 2018a: Restratification of abyssal mixing layers by submesoscale baroclinic eddies. *Journal of Physical Oceanography*, **48 (9)**, 1995–2010, https://doi.org/10.1175/JPO-D-18-0082.1.

Callies, J., 2018b: Restratification of Abyssal Mixing Layers by Submesoscale Baroclinic Eddies. *Journal of Physical Oceanography*, JPO–D–18–0082.1, https://doi.org/10.1175/

JPO-D-18-0082.1, URL http://journals.ametsoc.org/doi/10.1175/JPO-D-18-0082.1.

Capó, E., J. C. McWilliams, J. Gula, M. J. Molemaker, P. Damien, and R. Schubert, 2024: Abyssal Slope Currents. URL http://arxiv.org/abs/2402.11152.

Clément, L., and A. M. Thurnherr, 2018: Abyssal upwelling in mid-ocean ridge fracture zones. *Geophysical Research Letters*, **45 (5)**, 2424–2432.

Drake, H. F., R. Ferrari, and J. Callies, 2020: Abyssal circulation driven by near-boundary mixing: Water mass transformations and interior stratification. *Journal of Physical Oceanography*, **50 (8)**, 2203–2226, https://doi.org/10.1175/JPO-D-19-0313.1.

Drake, H. F., X. Ruan, J. Callies, K. Ogden, A. M. Thurnherr, and R. Ferrari, 2022a: Dynamics of eddying abyssal mixing layers over sloping rough topography. *Journal of Physical Oceanography*, **52 (12)**, 3199–3219.

Drake, H. F., X. Ruan, and R. Ferrari, 2022b: Diapycnal Displacement, Diffusion, and Distortion of Tracers in the Ocean. *Journal of Physical Oceanography*, **52 (12)**, 3221–3240, https://doi.org/10.1175/JPO-D-22-0010.1.

Drake, H. F., and Coauthors, 2025: Water mass transformation budgets in finite-volume generalized vertical coordinate ocean models. *Journal of Advances in Modeling Earth Systems*, **17 (3)**, e2024MS004 383.

Ferrari, R., A. Mashayek, T. J. McDougall, M. Nikurashin, and J. M. Campin, 2016: Turning ocean mixing upside down. *Journal of Physical Oceanography*, **46 (7)**, 2239–2261, https://doi.org/10.1175/JPO-D-15-0244.1.

Garrett, C., P. Maccready, and P. Rhines, 1993: BOUNDARY MIXING AND ARRESTED EKMAN LAYERS: ROTATING STRATIFIED FLOW NEAR A SLOPING BOUNDARY. Tech. rep., 291–323 pp. URL www.annualreviews.org.

Gevorgian, J., D. T. Sandwell, Y. Yu, S.-S. Kim, and P. Wessel, 2023: Global distribution and morphology of small seamounts. *Earth and Space Science*, **10 (4)**, e2022EA002 331.

Holmes, R. M., and T. J. McDougall, 2020: Diapycnal transport near a sloping bottom boundary. *Journal of Physical Oceanography*, **50 (11)**, 3253–3266, https://doi.org/10.1175/JPO-D-20-0066.1.

Ivey, G., K. Winters, and J. Koseff, 2008: Density stratification, turbulence, but how much mixing? *Annu. Rev. Fluid Mech.*, **40 (1)**, 169–184.

Khani, S., 2018: Mixing efficiency in large-eddy simulations of stratified turbulence. *Journal of Fluid Mechanics*, **849**, 373–394.

Lam, F.-P. A., L. R. Maas, and T. Gerkema, 2004: Spatial structure of tidal and residual currents as observed over the shelf break in the bay of biscay. *Deep Sea Research Part I: Oceanographic Research Papers*, **51 (8)**, 1075–1096.

Ledwell, J. R., A. J. Watson, and C. S. Law, 1998: Mixing of a tracer in the pycnocline. *Journal of Geophysical Research: Oceans*, **103 (C10)**, 21 499–21 529.

Legg, S., 2021: Mixing by Oceanic Lee Waves. *Annual Review of Fluid Mechanics*, **53**, 173–201, https://doi.org/10.1146/annurev-fluid-051220-043904.

Lien, R.-C., and E. A. D'Asaro, 2004: Lagrangian spectra and diapycnal mixing in stratified flow. *Journal of physical oceanography*, **34 (4)**, 978–984.

Lilly, D. K., 1962: On the numerical simulation of buoyant convection. *Tellus*, **14 (2)**, 148–172.

MacKinnon, J. A., and Coauthors, 2017: Climate Process Team on Internal Wave–Driven Ocean Mixing. *Bulletin of the American Meteorological Society*, **98 (11)**, 2429–2454, https://doi.org/10.1175/BAMS-D-16-0030.1, URL http://journals.ametsoc.org/doi/10.1175/BAMS-D-16-0030.1.

Marshall, J., D. Jamous, and J. Nilsson, 1999: Deep-Sea Research I. Tech. rep., 545–572 pp.

McDougall, T. J., and R. Ferrari, 2017: Abyssal upwelling and downwelling driven by near-boundary mixing. *Journal of Physical Oceanography*, **47 (2)**, 261–283, https://doi.org/10.1175/JPO-D-16-0082.1.

Muller, C. J., and O. Bühler, 2009: Saturation of the internal tides and induced mixing in the abyssal ocean. *Journal of Physical Oceanography*, **39 (9)**, 2077–2096.

Munk, W. H., 1966: Abyssal recipes. *Deep sea research and oceanographic abstracts*, Elsevier, Vol. 13, 707–730.

Nikurashin, M., and S. Legg, 2011: A mechanism for local dissipation of internal tides generated at rough topography. *Journal of Physical Oceanography*, **41 (2)**, 378–395, https://doi.org/10.1175/2010JPO4522.1.

Phillips, O., 1970: On flows induced by diffusion in a stably stratified fluid. *Deep sea research and oceanographic abstracts*, Elsevier, Vol. 17, 435–443.

Polzin, K., 2004: Idealized solutions for the energy balance of the finescale internal wave field. *Journal of Physical Oceanography*, **34 (1)**, 231–246.

Polzin, K., J. Toole, J. Ledwell, and R. Schmitt, 1997: Spatial variability of turbulent mixing in the abyssal ocean. *Science*, **276 (5309)**, 93–96.

Polzin, K. L., 2009: An abyssal recipe. *Ocean Modelling*, **30 (4)**, 298–309.

Ruan, X., and R. Ferrari, 2021: Diagnosing diapycnal mixing from passive tracers. *Journal of Physical Oceanography*, **51 (3)**, 757–767.

Ruan, X., Y. Si, and R. Ferrari, 2025: Diapycnal upwelling driven by tidally induced mixing over steep topography. *Journal of Physical Oceanography*, **55 (3)**, 229–241.

Sandwell, D. T., and Coauthors, 2022: Improved bathymetric prediction using geological information: Synbath. *Earth and Space Science*, **9 (2)**, e2021EA002 069.

Sarkar, S., and A. Scotti, 2017: From topographic internal gravity waves to turbulence. *Annual Review of Fluid Mechanics*, **49 (1)**, 195–220.

Schubert, R., J. Gula, E. Capó, P. Damien, J. Molemaker, C. Vic, and J. C. McWilliams, 2024: The ocean flows downhill near the seafloor and recirculates uphill above. URL https://www.researchsquare.com/article/rs-3872319/v1, https://doi.org/10.21203/rs.3.rs-3872319/v1.

Silvestri, S., G. L. Wagner, J.-M. Campin, N. C. Constantinou, C. N. Hill, A. Souza, and R. Ferrari, 2024: A new weno-based momentum advection scheme for simulations of ocean mesoscale turbulence. *Journal of Advances in Modeling Earth Systems*, **16 (7)**, e2023MS004 130.

Smagorinsky, J., 1963: General circulation experiments with the primitive equations: I. the basic experiment. *Monthly weather review*, **91 (3)**, 99–164.

St. Laurent, L., A. C. Naveira Garabato, J. R. Ledwell, A. M. Thurnherr, J. M. Toole, and A. J. Watson, 2012: Turbulence and diapycnal mixing in drake passage. *Journal of Physical Oceanography*, **42 (12)**, 2143–2152.

Taylor, G. I., 1922: Diffusion by continuous movements. *Proceedings of the london mathematical society*, **2 (1)**, 196–212.

Thurnherr, A. M., L. S. Laurent, R. Ferrari, T. Ijichi, and L. Clément, 2020: Transformation and upwelling of bottom water in fracture zone valleys. *Journal of Physical Oceanography*, **50 (3)**, 715–726, https://doi.org/10.1175/JPO-D-19-0021.1.

Vic, C., and Coauthors, 2019: Deep-ocean mixing driven by small-scale internal tides. *Nature communications*, **10 (1)**, 2099.

Wagner, G. L., and Coauthors, 2025: High-level, high-resolution ocean modeling at all scales with oceananigans. *arXiv preprint arXiv:2502.14148*.

Watson, A. J., J. R. Ledwell, M.-J. Messias, B. A. King, N. Mackay, M. P. Meredith, B. Mills, and A. C. Naveira Garabato, 2013: Rapid cross-density ocean mixing at mid-depths in the drake passage measured by tracer release. *Nature*, **501 (7467)**, 408–411.

Wenegrat, J. O., J. Callies, and L. N. Thomas, 2018: Submesoscale baroclinic instability in the bottom boundary layer. *Journal of Physical Oceanography*, **48 (11)**, 2571 – 2592, https://doi.org/10.1175/JPO-D-17-0264.1, URL https://journals.ametsoc.org/view/journals/phoc/48/11/jpo-d-17-0264.1.xml.

Whitley, V., and J. Wenegrat, 2025: Breaking internal waves on sloping topography: connecting parcel displacements to overturn size, interior-boundary exchanges, and mixing. *Journal of Physical Oceanography*, **55 (6)**, 645–661.

Wunsch, C., 1970: On oceanic boundary mixing. *Deep sea research and oceanographic abstracts*, Elsevier, Vol. 17, 293–301.

Wynne-Cattanach, B. L., and Coauthors, 2024: Observations of diapycnal upwelling within a sloping submarine canyon. *Nature*, **630 (8018)**, 884–890, https://doi.org/10.1038/s41586-024-07411-2.